Optics Letters

# Mid-infrared continua via spectral broadening and difference-frequency generation in a nanophotonic lithium niobate waveguide

Markus Ludwig,[1,2,8] Furkan Ayhan,[3] Thibault Voumard,[1,4] Weichen Fan,[1] Mahmoud A. Gaafar,[1,5] Victor Brasch,[6] Luis G. Villanueva,[3] and Tobias Herr[1,7,*]

[1]Deutsches Elektronen-Synchrotron DESY, Notkestr. 85, 22607 Hamburg, Germany
[2]Current address: University of Luxembourg, 162a Avenue de la Faïencerie, L-1511 Luxembourg and Institute for Advanced Studies, University of Luxembourg Campus Belval, L-4365 Esch-sur-Alzette, Luxembourg
[3]École Polytechnique Fédérale de Lausanne (EPFL), 1015 Lausanne, Switzerland
[4]Current address: Centre Suisse d'Électronique et de Microtechnique (CSEM), Rue Jaquet-Droz 1, 2002 Neuchâtel, Switzerland
[5]Current address: Technology Innovation Institute TII, Abu Dhabi, United Arab Emirates, and Department of Physics, Faculty of Science,Menoufia University, Egypt
[6]Q.ANT GmbH, Handwerkstraße 29, 70565 Stuttgart, Germany
[7]Physics Department, Universität Hamburg UHH, Luruper Chaussee 149, 22607 Hamburg, Germany
[8]markus.ludwig@uni.lu
*tobias.herr@desy.de

Received 9 December 2025; revised 21 February 2026; accepted 22 February 2026; posted 25 February 2026; published 17 March 2026

**Periodically poled thin film lithium niobate waveguides provide simultaneous access to efficient second- and third-order nonlinear processes, enabling broadband generation of coherent laser light. Here, we demonstrate the generation of a broadband mid-infrared continuum in a nanophotonic lithium niobate waveguide pumped by a telecom-wavelength femtosecond source. Specifically, our dual-stage design includes third-order nonlinear spectral broadening followed by a dedicated periodically poled waveguide section performing efficient broadband intrapulse difference-frequency generation. Driven by sub-100 fs pulses with an estimated on-chip pulse energy of around 200 pJ, the generated mid-infrared light covers wavelengths from 3200 to 4800 nm. Cascaded harmonic generation also extends the spectrum into the visible and ultraviolet domains, resulting in an overall spectral bandwidth ranging from 350 to 4800 nm.** 

https://doi.org/10.1364/OL.583084

**Introduction.** Access to coherent broadband light sources and frequency combs in the mid-infrared (MIR) [1–3] enables fundamental studies and catalyzes several technological applications. Among these are the exploration of ultrafast phenomena [4–6], molecular fingerprinting, trace gas sensing for environmental monitoring, and precision frequency metrology [7–9]. Using established near-infrared femtosecond lasers, broadband MIR generation is commonly obtained via $\chi^{(3)}$-based supercontinuum generation (SC) [10–12] or $\chi^{(2)}$ processes such as optical parametric oscillation (OPO) [13], optical parametric generation (OPG) [14,15] and difference-frequency generation (DFG) [16–23]. MIR combs generated via DFG, especially intrapulse DFG (IDFG), can be of zero carrier-envelope offset frequency [24,25], enabling the precise control of optical waveforms in the time domain and an elegant approach to absolute (SI time standard referenced) spectroscopy. MIR light generation via IDFG requires a broadband input spectrum that covers a large frequency interval $\Delta\nu$, since the process generates difference frequencies between spectral components of the input light. IDFG can then in principle, generate frequencies ranging from zero up to $\Delta\nu$, where in practice material absorption and dispersion often limit the achievable MIR bandwidth. For instance, to produce MIR light with wavelengths of 3 µm (100 THz), a pump pulse with a corresponding bandwidth of at least $\Delta\nu = 100$ THz is required. Previous work has already utilized bulk $LiNbO_3$ [26,27] and large mode-area waveguides [28,29] as a nonlinear medium for IDFG into the MIR. Its large second-order nonlinear coefficient and ferroelectricity enable efficient quasi-phase-matched second-order nonlinear processes and light conversion across multiple octaves, particularly when implemented as nanophotonic waveguides with sub-µm$^2$ cross-section [30–32]. Previous implementations of IDFG in $LiNbO_3$ have relied on spectral broadening in a nonlinear fiber [26–28,33,34] or nanophotonic waveguides [29], where the resulting supercontinuum is launched either into a bulk periodically poled $LiNbO_3$ (PPLN) crystal or large-area PPLN waveguide. This approach decouples the nonlinear broadening from the IDFG process, allowing the preparation of short and broadband input pulses before entering the dedicated DFG stage. In aluminum nitride waveguides, which like $LiNbO_3$ have large second- and third-order nonlinearities but without the possibility of periodic poling, spectral broadening and IDFG have been observed in the

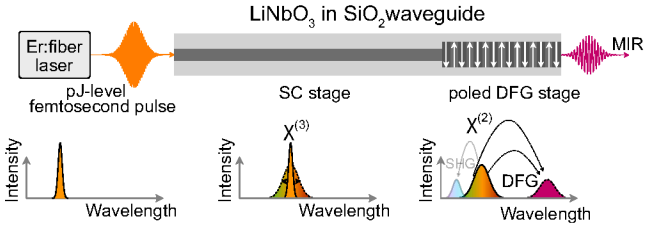


**Fig. 1. Concept of MIR generation in a dual-stage lithium niobate waveguide.** A femtosecond pulse from an Er:fiber laser first undergoes supercontinuum generation (SC) via $\chi^{(3)}$, followed by quasi-phase-matched difference-frequency generation (DFG) via $\chi^{(2)}$ (with possible harmonic generation).

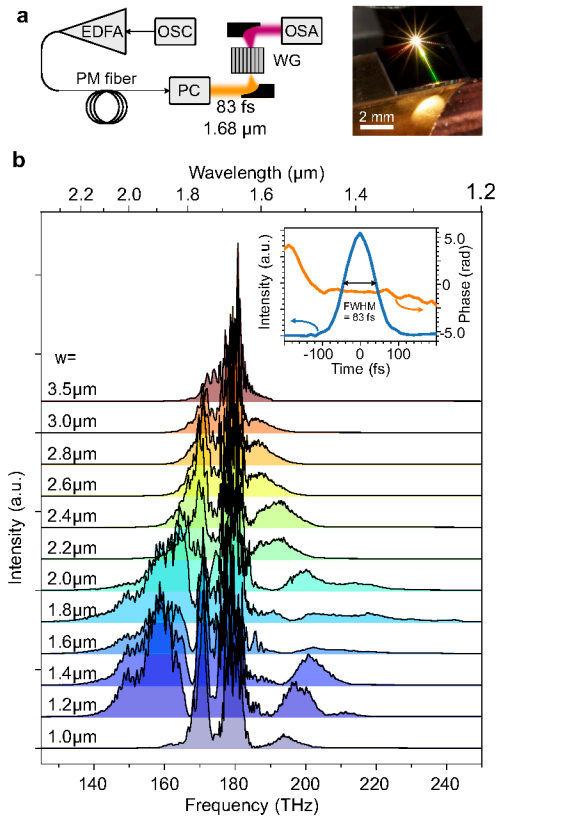


**Fig. 2. Supercontinuum generation in an unpoled $LiNbO_3$ waveguide.** (a) Experimental setup. EDFA, Er:fiber amplifier; OSA, optical spectrum analyzer; OSC, femtosecond laser; PC, prism compressor; photograph, $LiNbO_3$ waveguide in operation; PM fiber, 1 m of standard polarization-maintaining fiber. (b) Supercontinua in $LiNbO_3$ waveguides without poling at an estimated on-chip pulse energy of 300 pJ, as a function of waveguide (top) width. A bandwidth exceeding 100 THz at the 10% intensity level can be achieved (spectra shown here on a linear intensity scale). Inset: reconstructed pulse parameters based on SHG-FROG.

same waveguide, indicating potential for compact MIR sources [35].

Here, we explore the integration of both spectral broadening (supercontinuum generation) and IDFG into a single monolithic dual-stage nanophotonic $LiNbO_3$ waveguide [36,37] (see Fig. 1). The IDFG section in particular incorporates broadband quasi-phase-matching via periodic poling. Based on this structure, we demonstrate MIR light generation from a femtosecond

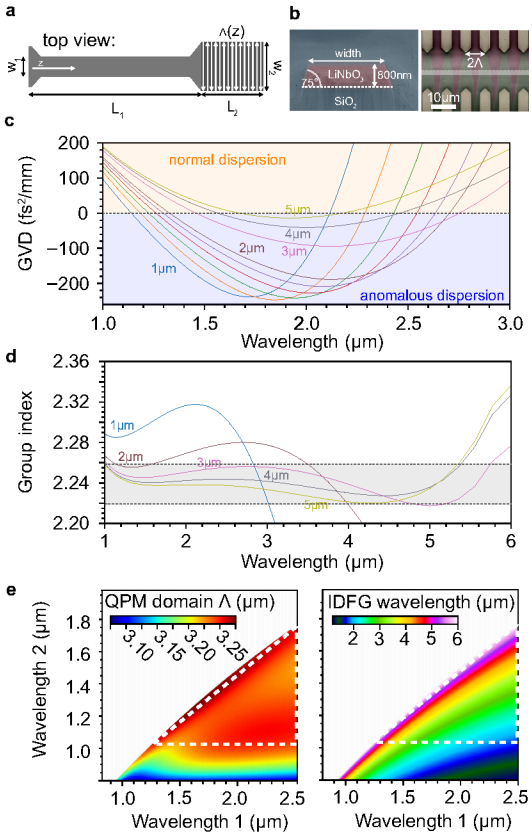


**Fig. 3. Waveguide design.** (a) Dual-stage waveguide with a narrow supercontinuum section and subsequent wider periodically poled IDFG section for minimal temporal walk-off and improved long-wavelength mode confinement. (b) Scanning electron micrograph of a waveguide cross-section and of the poled material before etching (with electrodes for poling). The horizontal light gray bar indicates the location of the later etched waveguide. (c) Calculated group velocity dispersion as a function of wavelength for different waveguide top widths; curves from 1 to 2 μm are shown in 0.2 μm increments. (d) Calculated group index as a function of wavelength for different waveguide widths. (e) Calculated quasi-phase-matching for a waveguide width of 3000 nm. Left: color-coded domain width (half poling period) as a function of two input wavelengths (1 & 2) driving IDFG. Right: resulting output IDFG wavelengths as a function of the two input wavelengths. The nearly constant color code inside the dashed triangle (left graph) indicates a nearly uniform requirement for the poling period for IDFG output wavelengths between 3 μm and 6 μm (right graph).

Er:fiber laser: Tailoring the group velocity dispersion (GVD) optimizes the efficiency and spectral extent of the supercontinuum generation, whereas group index matching and quasi-phase-matching are key for maximizing the IDFG efficiency.

**Results.** Figure 2(a) shows the experimental setup. As a pump source, we use a homemade Er:fiber laser [38,39] with a repetition rate of 40 MHz. After amplification in an Er:fiber amplifier to 300 mW average power (7.5 nJ pulse energy), the pulses propagate through 1 m of standard polarization-maintaining (PM) 1550 nm fiber, where 83 fs Raman-shifted soliton pulses with a central wavelength of 1680 nm are generated. We isolate these well-defined light pulses via spectral filtering to suppress any non-solitonic component (not Raman-shifted) via a free-space silicon prism compressor setup configured for zero net disper-

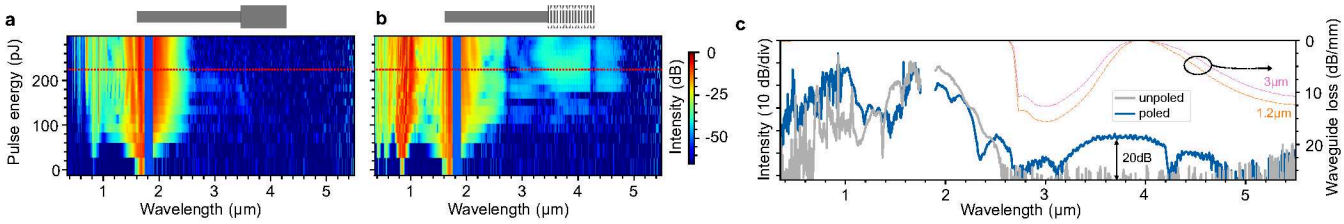


**Fig. 4. MIR comb generation via IDFG.** (a) Output spectra of an unpoled waveguide as a function of estimated on-chip input pulse energy. (b) Output spectra of an identical waveguide geometry as in (a) but with periodic poling. Spectral slices at 236 pJ (red dotted lines) are shown in panel (c). The dashed lines indicate waveguide losses calculated for the two involved waveguide widths.

sion. This configuration also permits tuning of the optical pulse energy via a variable neutral-density filter without affecting pulse duration or chirp. The maximum available soliton pulse energy measured directly before coupling into the waveguide is 2.3 nJ at an average power of 92 mW. Off-axis parabolic mirrors couple the pulses into the waveguide and collimate the output light achromatically. Assuming a coupling efficiency per facet of 13% (see below), this provides a maximum estimated on-chip pulse energy of 300 pJ. The inset in Fig. 2(b) shows the reconstructed pulse based on second-harmonic generation frequency-resolved optical gating (SHG-FROG) [40].

First, to design the initial spectral broadening stage, we fabricate a series of $SiO_2$ cladded, unpoled $LiNbO_3$ on insulator (LNOI) waveguides of different (top) widths, a fixed side wall angle of 75°, a film thickness of 800 nm (see SEM image in Fig. 3(b)) and overall length of 5 mm [41]. The crystal axis is oriented such that it aligns with the transverse electric (TE) mode. With these waveguides, we perform supercontinuum generation with the highest available on-chip pulse energy of 300 pJ to identify the optimum between dispersion-limited spectral broadening and enhanced nonlinearity due to the mode confinement. Figure 2(b) shows the resulting spectra on a linear intensity scale as a function of frequency. The widest spectral broadening is achieved for waveguide widths between 1 μm to 2 μm, reaching spectral bandwidths beyond 100 THz. In our case, we select a waveguide width of 1.2 μm, providing a broadband spectrum while still avoiding spectral overlap between the expected IDFG comb and the fundamental comb. In addition, we simulate waveguide dispersion via the finite element method (FEM) based on commonly available bulk material data [42,43]. Figure 3(c) illustrates the resulting GVD for different waveguide widths. Anomalous dispersion—a requirement for broadband supercontinuum generation via self-compression—can be achieved for all widths. Values between 1 μm to 2 μm maximize the spectral width of the anomalous dispersion region centered close to the pump wavelength, consistent with the experimental observations.

Second, for optimal IDFG efficiency, the temporal overlap of all frequency components along the DFG stage is important. Figure 3(d) shows the group index for different waveguide geometries based on the dispersion simulation. The lowest variation in the group index of less than 1% across a spectral bandwidth of 1 μm to 5 μm is achieved for waveguide widths between 3 μm to 5 μm. To maximize nonlinearity, we choose a width of 3 μm. In addition to group index matching, phase matching is a critical requirement, which we approach here through periodic poling: Fig. 3(e) visualizes the quasi-phase-matching (QPM) conditions for the poling domain width $\Lambda = \frac{\pi}{\Delta k}$ as a function of possible combinations of two input wavelengths. The left panel indicates the domain width (half poling period) while the right panel indicates the resulting DFG wavelength. Interestingly, DFG output wavelengths from 3 μm to 6 μm (see dashed triangle in Fig. 3(e)) can be achieved with a nearly uniform domain width of $3.25 \pm 0.05$ μm (poling period of $6.5 \pm 0.1$ μm). At the cost of a possibly reduced conversion efficiency, we choose a linearly chirped poling, covering periods from 6.3 μm to 6.8 μm, to accommodate potential fabrication imperfections. We also note that the QPM period for SHG phase matching is relatively similar at 6.2 μm. The final design of the dual-stage waveguide is illustrated in Fig. 3(a). Out of the total waveguide length of 5 mm, we dedicate the first 4 mm ($L_1$) to spectral broadening, and 1 mm ($L_2$) to IDFG. The waveguide width at the chip's input facets is 2.5 μm and tapers over a distance of 200 μm down to $w_1 = 1.2$ μm. The output facet width equals the width of the DFG stage $w_2 = 3$ μm, and the taper between the narrow and wide waveguide sections extends over 250 μm. We record the output spectra versus input pulse energy using two optical spectrum analyzers (Yokogawa AQ6377/AQ6374). The resulting spectra are shown in Figs. 4(a) and 4(b), and are recorded with identical waveguide geometry under the same coupling conditions, with the sole distinction that the sample in Fig. 4(b) is periodically poled. The unpoled waveguide does not generate detectable light beyond a wavelength of 2.5 μm. In contrast, the poled waveguide exhibits significant light conversion into a wide window between 3 μm and 4.8 μm. The roll-off beyond 4.8 μm correlates with simulated propagation loss from FEM mode calculations including silica-cladding overlap (Fig. 4(c), right axis). For both the SC (1.2 μm) and DFG (3.0 μm) sections, it exceeds 10 dB/mm for $\lambda > 5$ μm. The feature between 2.5 μm and 3.5 μm arises from the OH absorption band, while a narrower dip near 4.2 μm is consistent with $CO_2$ absorption. The spectra also show efficient higher-harmonic generation. We attribute this to higher poling order and mode order phase matching and non-symmetric poling (i.e., imperfect 50:50 duty cycle). Figure 4(c) shows spectral slices corresponding to the dotted red lines of Figs. 4(a) and 4(b) at an on-chip pulse energy of 236 pJ. This value yields the maximum MIR output, enhanced by at least 20 dB compared to the unpoled structure. As seen in Fig. 4(b), MIR emission is weaker at lower pulse energies despite similar NIR bandwidth, while at higher pulse energies the MIR signal decreases again, consistent with IDFG and indicating an optimal operating point set by temporal overlap in the poled section. Based on a broadband thermal powermeter (Newport 843-R/919P-003-10 detector head), the total collimated off-chip output power, corresponding to the spectrum in Fig. 4(c) for the poled waveguide, amounts to 1.22 mW. Comparison with the off-chip input power of 72 mW measured on the same thermal powermeter allows us to determine the transmission to be at

least 1.7%. This corresponds to a total insertion loss of approximately 18 dB. Assuming a symmetric coupling, this translates to a coupling efficiency of 13% per facet, in line with earlier measurements [32]. While we expect that this approximation represents the coupling efficiency well at the pump wavelength (which still dominates the spectrum), the MIR coupling efficiency is likely lower, so that our estimates for the generated MIR power are conservative lower bounds: The on-chip power contained in the entire spectrum shown in Fig. 4(c) is 9 mW. By integration, we determine the on-chip power contained in the MIR portion (3.2 µm to 4.8 µm) to be 23 µW, indicating a conversion efficiency on the order of 0.2%. The IDFG-based MIR spectrum, spectrally separated from the pump supercontinuum, could in principle constitute a frequency comb with zero carrier-envelope offset frequency. However, recent studies show that spectral overlap between the fundamental supercontinuum and its second-harmonic (which is the case here) can generate interleaved combs with non-zero offset frequency across the entire spectrum [44]; thus, further studies are needed to clarify the spectral structure of the MIR spectra.

**Conclusion.** In conclusion, we demonstrate MIR generation from a telecom-wavelength Er:fiber laser through supercontinuum generation and subsequent IDFG, both realized in a single 5 mm nanophotonic $LiNbO_3$ waveguide. Quasi-phase-matching via periodic poling enables MIR emission spanning 3.2 to 4.8 µm at input on-chip pulse energies of about 200 pJ. Future work may improve coupling efficiency, explore different cladding materials with lower MIR absorption, and investigate the spectral structure of the IDFG output, in particular its carrier-envelope offset frequency [44]. Overall, our results establish a direct link between the telecom and MIR bands for integrated photonics.

**Funding.** Swiss National Science Foundation (193689); European Research Council (853564); HORIZON EUROPE European Innovation Council (101046920); Helmholtz Association (VH-NG-1404); Partnership for Innovation, Education, and Research of Universität Hamburg and DESY (PIF-2022-09).

**Acknowledgment.** The $LiNbO_3$ waveguides were fabricated in the EPFL Center of MicroNanoTechnology (CMi). The work was supported through the Maxwell computational resources operated at DESY. We thank Yokogawa Deutschland GmbH for lending us the AQ6377.

**Disclosures.** The authors declare no conflicts of interest.

**Data availability.** The datasets analyzed during the current study are available from the corresponding authors upon reasonable request.

## REFERENCES

1. I. T. Sorokina and K. L. Vodopyanov, eds., in *Topics in Applied Physics* (Springer, 2003), Vol. **89**.
2. A. Schliesser, N. Picqué, and T. W. Hänsch, Nat. Photonics **6**, 440 (2012).
3. Y. Zhang, K. Wu, Z. Guang, *et al.*, Laser Photonics Rev. **18**, 2300786 (2024).
4. A. A. Lanin, A. A. Voronin, A. B. Fedotov, *et al.*, Sci. Rep. **4**, 6670 (2014).
5. H. Pires, M. Baudisch, D. Sanchez, *et al.*, Prog. Quantum Electron. **43**, 1 (2015).
6. C. Schoenfeld, L. Feuerer, A. Heinrich, *et al.*, Laser Photonics Rev. **18**, 2301152 (2024).
7. S. A. Diddams, K. Vahala, and T. Udem, Science **369**, eaay3676 (2020).
8. N. Picqué and T. W. Hänsch, Nat. Photonics **13**, 146 (2019).
9. T. Fortier and E. Baumann, Commun. Phys. **2**, 153 (2019).
10. T. Sylvestre, E. Genier, A. N. Ghosh, *et al.*, J. Opt. Soc. Am. B **38**, F90 (2021).
11. I. Zorin, P. Gattinger, A. Ebner, *et al.*, Opt. Express **30**, 5222 (2022).
12. C.-S. Brès, A. D. Torre, D. Grassani, *et al.*, Nanophotonics **12**, 1199 (2023).
13. A. V. Muraviev, V. O. Smolski, Z. E. Loparo, *et al.*, Nat. Photonics **12**, 209 (2018).
14. V. Petrov, Opt. Mater. **34**, 536 (2012).
15. B. Hu, X. Yang, J. Wu, *et al.*, Nat. Commun. **14**, 7125 (2023).
16. A. Bonvalet, M. Joffre, J. L. Martin, *et al.*, Appl. Phys. Lett. **67**, 2907 (1995).
17. R. A. Kaindl, D. C. Smith, M. Joschko, *et al.*, Opt. Lett. **23**, 861 (1998).
18. C. Erny, K. Moutzouris, J. Biegert, *et al.*, Opt. Lett. **32**, 1138 (2007).
19. C. Gaida, M. Gebhardt, T. Heuermann, *et al.*, Light. Sci. Appl. **7**, 94 (2018).
20. G. Ycas, F. R. Giorgetta, E. Baumann, *et al.*, Nat. Photonics **12**, 202 (2018).
21. A. J. Lind, A. Kowligy, H. Timmers, *et al.*, Phys. Rev. Lett. **124**, 133904 (2020).
22. F. Ritzkowsky, E. Bebeti, G. M. Rossi, *et al.*, Opt. Lett. **48**, 1870 (2023).
23. Q. Bournet, M. Jonusas, F. Guichard, *et al.*, Appl. Phys. B **130**, 33 (2024).
24. A. Baltuška, T. Fuji, and T. Kobayashi, Phys. Rev. Lett. **88**, 133901 (2002).
25. G. Krauss, D. Fehrenbacher, D. Brida, *et al.*, Opt. Lett. **36**, 540 (2011).
26. D. M. B. Lesko, H. Timmers, S. Xing, *et al.*, Nat. Photonics **15**, 281 (2021).
27. N. Hoghooghi, S. Xing, P. Chang, *et al.*, Light. Sci. Appl. **11**, 264 (2022).
28. A. S. Kowligy, A. Lind, D. D. Hickstein, *et al.*, Opt. Lett. **43**, 1678 (2018).
29. A. S. Kowligy, D. R. Carlson, D. D. Hickstein, *et al.*, Opt. Lett. **45**, 3677 (2020).
30. C. Wang, C. Langrock, A. Marandi, *et al.*, Optica **5**, 1438 (2018).
31. T.-H. Wu, L. Ledezma, C. Fredrick, *et al.*, Nat. Photonics **18**, 218 (2024).
32. M. Ludwig, F. Ayhan, T. M. Schmidt, *et al.*, Nat. Commun. **15**, 7614 (2024).
33. K. Iwakuni, S. Okubo, O. Tadanaga, *et al.*, Opt. Lett. **41**, 3980 (2016).
34. W. Hettel, G. Golba, D. Morrill, *et al.*, Opt. Express **32**, 4072 (2024).
35. D. D. Hickstein, H. Jung, D. R. Carlson, *et al.*, Phys. Rev. Appl. **8**, 014025 (2017).
36. T.-H. Wu, P. Chang, and S. A. Diddams, in *Optica Nonlinear Optics Topical Meeting 2023* (Optica Publishing Group, 2023), paper Th2A.7.
37. T.-H. Wu, P. Chang, and S. A. Diddams, in *Conference on Lasers and Electro-Optics (CLEO) 2025* (Optica Publishing Group, 2025), paper SS100_1.
38. J. D. Kafka, D. W. Hall, and T. Baer, Opt. Lett. **14**, 1269 (1989).
39. D. Brida, G. Krauss, A. Sell, *et al.*, Laser Photonics Rev. **8**, 409 (2014).
40. K. W. DeLong, R. Trebino, J. Hunter, *et al.*, J. Opt. Soc. Am. B **11**, 2206 (1994).
41. F. Ayhan, M. Ludwig, T. Herr, *et al.*, APL Photonics **10**, 016118 (2025).
42. D. E. Zelmon, D. L. Small, and D. Jundt, J. Opt. Soc. Am. B **14**, 3319 (1997).
43. I. H. Malitson, J. Opt. Soc. Am. **55**, 1205 (1965).
44. W. Fan, F. Ayhan, T. Wildi, *et al.*, Phys. Rev. Lett. **135**, 213801 (2025).